Acta Cryst B
STRUCTURAL SCIENCE
CRYSTAL ENGINEERING
MATERIALS
ISSN 2052-5206

Charge density and optical properties of multicomponent crystals containing active pharmaceutical ingredients or their analogues

Marlena Gryl*

Department of Crystal Chemistry and Crystal Physics, Jagiellonian Univeristy, Kraków 30-060, Poland.
*Correspondence e-mail: gryl@chemia.uj.edu.pl

Received 7 January 2015
Accepted 14 July 2015

Edited by M. de Boissieu, SIMaP, France

Keywords: crystal engineering; active pharmaceutical ingredients; charge density studies; optical properties; *ab initio* calculations.

Supporting information: this article has supporting information at journals.iucr.org/b

Active pharmaceutical ingredients (APIs), through their favourable donor/acceptor spatial distribution and synthon formation flexibility, are attractive building blocks in modern materials crystallography. The optical properties of a crystal strongly depend on two factors, *i.e.* the spatial distribution of molecules in the crystal structure and the electronic properties of molecular building blocks (dipole moments, polarizabilities, hyperpolarizabilities). Although the latter are easy to predict through *ab initio* calculations, the former are not. Only a combination of experimental and theoretical charge density studies together with prediction and measurement of optical properties enable full analysis of the obtained functional material in terms of its usefulness in practical applications. This article presents design strategies of optical materials based on selected pharmaceutical molecules. Factors that contribute to molecular recognition in the four selected polar/chiral crystal phases (derived through charge density and Hirshfeld surfaces analysis) have been determined. Theoretically predicted optical properties of the molecular/ionic building blocks as well as bulk effects have been confirmed experimentally. This research is a first step in the design of novel optical materials based on push–pull molecules and APIs.

1. Introduction

Molecular self-assembly leading to crystalline materials showing unique physical properties is a complicated process, which requires understanding of the molecular/atomic features of the building blocks constituting the crystal phase. Quantitative crystal engineering (Tiekink *et al.*, 2011) combines experimental and theoretical techniques which enable moving from trial-and-error to comprehensive solutions in materials crystallography. The following methods should be of particular interest for the design of solids with desired physical, chemical or biological properties:

(i) X-ray single-crystal diffraction and structural analysis provides information on the molecular conformation and mutual arrangement of building blocks within the crystal structure.

(ii) Charge density studies allow the evaluation of inter- and intramolecular interactions in the context of crystal packing (Munshi & Row, 2005).

(iii) *Ab initio* calculations of the molecular/atomic properties of the molecules/ions building the structure, which gives hope for predicting the bulk properties (there is no direct correlation between molecular polarizabilities/hyperpolarizabilities and bulk properties of the crystal).

In particular, the optical properties of a crystal depend on the spatial distribution of molecules in the crystal structure, as well as on the electronic properties (dipole moment, polariz-

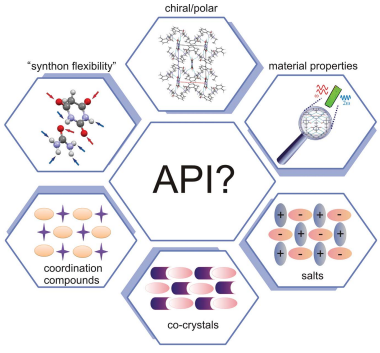

ability, hyperpolarizability) of the building blocks. Optical devices serve a major role in modern sciences and technology. Several requirements are necessary for the successful design of optical materials to take place. In particular, crystal phases engineered towards linear and non-linear optical properties are often bound by symmetry restrictions: structural polarity and/or chirality. Properties like optical activity (OA) or second harmonic generation (SHG) can be observed only in noncentrosymmetric crystals (Boulanger & Zyss, 2003). Additionally, for an outstanding bulk effect molecular or ionic building blocks should possess large values of polarizability and/or hyperpolarizability. The synthesis of such materials is still challenging. Many organic molecules with high polarizability and hyperpolarizability arrange into dimers or have an antiparallel orientation in the crystal structure, in both cases causing dipole moments to cancel themselves out (Stadnicka *et al.*, 2002). In this case the crystal structure does not exhibit desirable bulk properties such as OA or SHG. In the structure, enhancement of the dipole moment by a controlled alignment of building blocks is very much possible and favorable for a sufficient bulk effect to take place. A charge density study of the non-linear optical (NLO) chromophore 2-methyl-4-nitroaniline has shown the significance of this effect (Howard *et al.*, 1992; Whitten *et al.*, 2006).

There are many ways to overcome the centrosymmetricity barrier: usage of chiral molecules or chiral solvents for crystallization and co-crystallization; utilization of co-crystal formers that promote the formation of noncentrosymmetric crystal structures (Cole, 2003). Even if the structure lacks an inversion center, pure organic, single component molecular materials despite having generally large nonlinear optical susceptibilities of second order have certain limitations: poor mechanical resistance and increased optical absorption. The solution for modern optoelectronics seems to be multi-component materials built of either organic or mixed organic and inorganic components selected in a specific way in order to combine molecular and structural properties to form a three-dimensional architecture. The choice of building blocks is crucial: in an ideal case push–pull molecules should be linked with constituents enabling synthon formation flexibility. In the search for hydrogen-bond diversity one could consider active pharmaceutical ingredients (APIs). An API is a substance or a mixture of substances used in the manufacture of a drug product and which becomes an active ingredient in the drug product itself. Interest in pharmaceutical molecules has so far been focused on modifying the bioavailability, safety and efficacy of the drug product. One might wonder why APIs? There are many other molecules with hydrogen-bond donor and acceptor sites. First of all we should not consider APIs as one hermetic group with similar or identical functional groups. APIs can be simple molecules like urea or more complex systems like lidocaine or quinidine. What makes them worth considering is: (1) availability – many of them (despite a general belief) are easily accessible as they are used in the pharmaceutical industry; (2) price – low cost compared with other organic molecules with a complex, multistep synthesis and/or not synthesized on an industrial scale; (3) toxicity – less harmful compared with many organic compounds, *e.g.* 2-amino-5-nitropyridine, 2-methyl-4-nitroaniline, 4-nitroaniline and others proposed as NLO chromophores; (4) chirality – some APIs possess one or more chiral centers, promoting the formation of polar/chiral crystal structures; (5) polymorphism – many APIs crystallize in many polymorphic forms ensuring synthon formation flexibility, which is relevant for crystal engineering; (6) scientifically scrutinized – pharmaceutical co-crystals and salts are gaining more and more attention in the scientific community, thus already there is a sufficient amount of structural data for crystal engineering purposes; (7) the fact that there are crystals of API or their derivatives known to exhibit NLO effects. Barbituric acid derivatives are known as organic, efficient NLO materials, *e.g.* tetrathiafulvalene-*n*-(thio)barbituric acid chromophores or glucosyl substituted barbituric acid derivatives (Song *et al.*, 1995; Cao *et al.*, 1995; Garín *et al.*, 1998; Vohra *et al.*, 2000; Pal *et al.*, 2001; Lee *et al.*, 2005; Feng *et al.*, 2006). In particular, *p*-substituted benzalbarbituric acids were found to exhibit relatively high SHG intensity (Kondo *et al.*, 1990, 1991, 1992) and exceptional hardness in comparison with other organic materials used for SHG measurements. Toth *et al.* (2015) predicted theoretically a SHG effect for several API crystals (*e.g.* crystals of quinidine, flutamide, griseofulvin, benzocaine, naproxen and others) in the search for an effective way to probe the crystal structures of pharmaceutically relevant solids. Moreover, urea crystals are used as standard for SHG measurements.

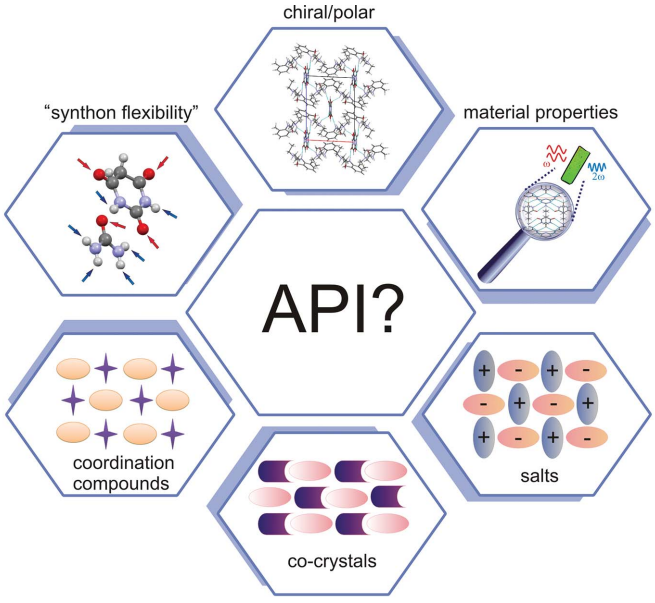

Figure 1
APIs in the design of multi-component functional solids.

APIs have already proven useful for designing multi-component functional solids utilizing the favorable spatial distribution of hydrogen-bond donors and acceptors in the molecule (Gryl *et al.*, 2014), see Fig. 1. The ability to form heterosynthons with other molecules could be used for engineering crystal phases exhibiting a wider scope of properties and in particular linear and nonlinear optics (LO and NLO,

resxpectively; Gryl *et al.*, 2015). Different utilization of the same donors and acceptors of hydrogen bonds leads to a variety of salts, co-crystals, coordination compounds and solvates based on API molecules (Vishweshwar *et al.*, 2005). There are known attempts to introduce polarity and/or chirality to the crystal structure and tuning of mechanical properties through co-crystallization with APIs. Urea and *m*-nitrobenzoic acid co-crystals (Rai *et al.*, 2002) have a SHG intensity comparable with that of urea, whereas the hardness of the material is much improved in the binary crystal. Two out of three pharmaceutical co-crystals of 1,4-bis(4-pyridyl)-2,3-diaza-1,3-butadiene and camphoric acid are non-centrosymmetric (Bisht *et al.*, 2014) and are built of optically active, flexible organic nitrogen-donor molecules. Co-crystals and salts of amino acids are known NLO materials: L-ornithine monohydrochloride (Senthil *et al.*, 2009) L-phenylalanine-benzoic acid co-crystals, LPBA (Geetha *et al.*, 2011); glycine oxalic acid co-crystals, GOA (Pandey, 2014); glycine thiourea co-crystals, GT (Ruby & Raj, 2013); L-histidinium hydrogen oxalate (Chimpri *et al.*, 2013). Co-crystals containing salicylic acid (Andal & Murugakoothan, 2014) and nicotinamide or izonicotinamide (Ratajczak *et al.*, 2013) are known to exhibit NLO effects. Bis nicotinamidium bis D-tartrate 1.25-hydrate crystals exhibit SHG efficiency of 1.25 compared with KDP (potassium dihydrogen phosphate) (Senthil Murugan *et al.*, 2015). A favorable distribution of hydrogen-bond donors and acceptors as well as the possibility of metal-ion complexation (Bolz *et al.*, 2010) allow the potential for the designed engineering of novel materials based on barbituric acid or its derivatives (Zerkowski *et al.*, 1997; Lehn *et al.*, 1990; Xiong *et al.*, 2003). All of the above facts make pharmaceutical molecules at least worth considering as components for engineering optical devices.

Table 1
Crystal data and structure refinement for lid.

Crystal data	
Chemical formula	$C_{14}H_{22}N_2O$
M_r	234.33
Crystal system, space group	Monoclinic, $P2_1$
Temperature (K)	112
a, b, c (Å)	12.8666 (1), 13.6966 (1), 16.2049 (1)
β (°)	100.686 (1)
V (Å^3)	2806.24 (4)
Z	8
$F(000)$	1024
D_x (Mg m^{-3})	1.109
Radiation type	Mo $K\alpha$
μ (mm^{-1})	0.07
Crystal size (mm)	0.40 × 0.25 × 0.15
Data collection	
Diffractometer	SuperNova, Dual, Cu at zero, Atlas
Absorption correction	Multi-scan, *CrysAlis Pro*
T_{min}, T_{max}	0.845, 1.000
No. of measured, independent and observed [$I > 2\sigma(I)$] reflections	32 520, 16 346, 12 599
R_{int}	0.0384
θ values (°)	θ_{max} = 30.0, θ_{min} = 3.0
Completeness to θ (%)	99.8
$(\sin\theta/\lambda)_{max}$ (Å^{-1})	0.703
Refinement†	
$R[F^2 > 2\sigma(F^2)]$, $wR(F^2)$, S	0.046, 0.119, 1.06
No. of reflections	16 346
No. of parameters	641
No. of restraints	5
H-atom treatment	H atoms treated by a mixture of independent and constrained refinement
$\Delta\rho_{max}$, $\Delta\rho_{min}$ (e Å^{-3})	0.22, −0.21
Absolute structure parameter	0.4 (3)‡

† Sheldrick (2015) ‡ Because the structure contains exclusively light atoms, absolute structure cannot be determined reliably.

After the selection of building blocks based on the predicted lock-and-key mechanism, their properties and how they are affected by the crystal field can be assessed. The Quantum Theory of Atoms in Molecules (QTAIM) allows the characterization of interactions in crystals through analysis of concentration and depletion of electron density (Bader, 1990; Matta & Bader, 2006). Topological and energetic descriptors can yield the means for distinguishing closed-shell and shared-shell systems (Mallinson *et al.*, 2003; Espinosa *et al.*, 1999). The classification of intra- and intermolecular interactions is vital for crystal engineering and thus we need to go further than what is offered by classical X-ray diffraction. In principle, we need to know as much about the electronic properties of the building blocks as their ability to form crystal structures. Electron density studies both of the components and their crystal structures allow us closer to finding out what determines the outcome of the engineering process. Charge density studies gave an insight into the salt and co-crystal formation for two crystal phases based on nicotinamide (Hathwar *et al.*, 2010). The topological analysis of urea–barbituric acid co-crystal polymorphs led to the conclusion that the shift of electron density towards a specific mesomeric form is responsible for the creation of synthon polymorphism (Gryl *et al.*, 2011). Hathwar *et al.* (2011) discussed synthon modularity and proposed the production of a transferable databank of multipolar parameters for charge density studies to use as a new tool for quantitative crystal engineering. In particular, research on transferable multipolar parameters towards applications in chemical crystallography has been carried out by several research groups (Dittrich *et al.*, 2006; Dominiak *et al.*, 2007; Chimpri & Macchi, 2013; Hübschle *et al.*, 2007; Jelsch *et al.*, 1998; Volkov *et al.*, 2007; Zarychta *et al.*, 2007). There are only a few examples of the application of the charge density method to crystal engineering described recently in Krawczuk & Macchi (2014).

The next step after obtaining the crystal structure and prior to the experimental measurements should be the estimation of optical properties based on calculations of molecular/ionic polarizabilities, hyperpolarizabilities, refractive indices and linear and second-order nonlinear electric susceptibilities for crystals. The description of a variety of approaches available is not a subject of this paper. Let me just summarize that modern *ab initio* quantum chemical methods based on the coupled perturbed Kohn Sham (CPKS) approach give a reasonable approximation of static values of polarizability, hyperpolarizability, refractive indices and linear and non-linear electric susceptibilities (Dovesi, Orlando, Erba *et al.*, 2014). One can account for the external electric field and internal crystal field

effects using the modified rigorous local field theory (RLFT) approximation proposed by Seidler *et al.* (2014).

A final result of the engineering process is a material with the desired predicted properties and their validation. In this paper four different crystal phases will be presented: salts, co-crystals and coordination compounds all based on barbituric acid/barbiturates. Understanding their crystal structure and properties is a step towards obtaining more efficient optical materials with incorporated push–pull molecules as NLO chromophores.

2. Results and discussion

2.1. Lidocaine barbiturate

Lidocaine barbiturate (lidbar) is a representative of organic salt crystals, which are nowadays considered to be the most promising organic NLO materials. Details of the crystallization have been previously described by Gryl *et al.* (2013). Crystals of lidbar belong to a polar/chiral space group $P2_1$, and have two barbiturate anions and two lidocaine cations in the asymmetric unit (Fig. 2). There is a slight difference in the conformations of the lidocaine ions (Fig. S1), whereas the geometries of the two barbiturate ions *A* and *B* are almost identical. Each molecule/ion in the crystal structure has its unique environment related to the interactions with neighboring species. Mapping of these interactions on a two-dimensional plot (McKinnon *et al.*, 1998, 2007) gives a unique fingerprint of the molecule/ion and enables their quantification. Closer inspection of intermolecular interactions through Hirshfeld surfaces analysis revealed discrepancies in fingerprint plots for both cations and ions (Fig. 3). In particular, a wide spread of points from 0.8 to 2.4 Å for d_e and d_i can be attributed to several different interactions in the examined structure (Table S1). The fingerprints for the barbituric ions (Figs. 3*a* and *b*) show two spikes pointing to the lower left side of the drawing, indicating the presence of O···H interactions. Sets of diffuse points between the spikes are from H···H contacts within the dimers formed by barbiturate ions. The upper wing-shaped features can be attributed to C—H···π interactions. In anion *B* (Fig. 3*b*) the upper part of the plot is irregular and elongated which can be attributed to a long C5*B*—H5*B*···π contact of 3.73 Å. Fingerprint plots for lidocaine ions can be interpreted in a similar way

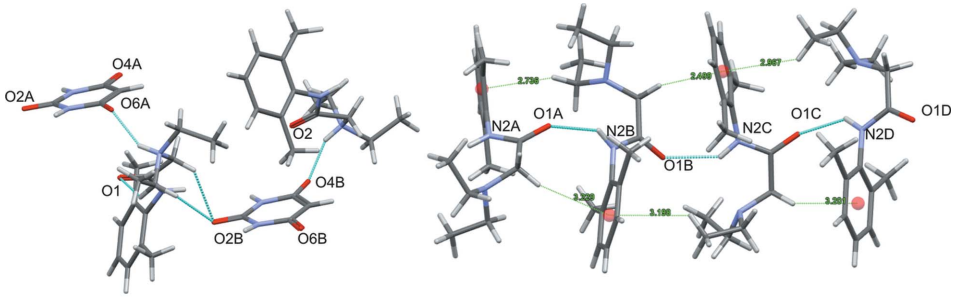

Figure 2
Contents of the asymmetric unit for (*a*) lidbar and (*b*) lid with marked hydrogen bonds and C—H···π between species.

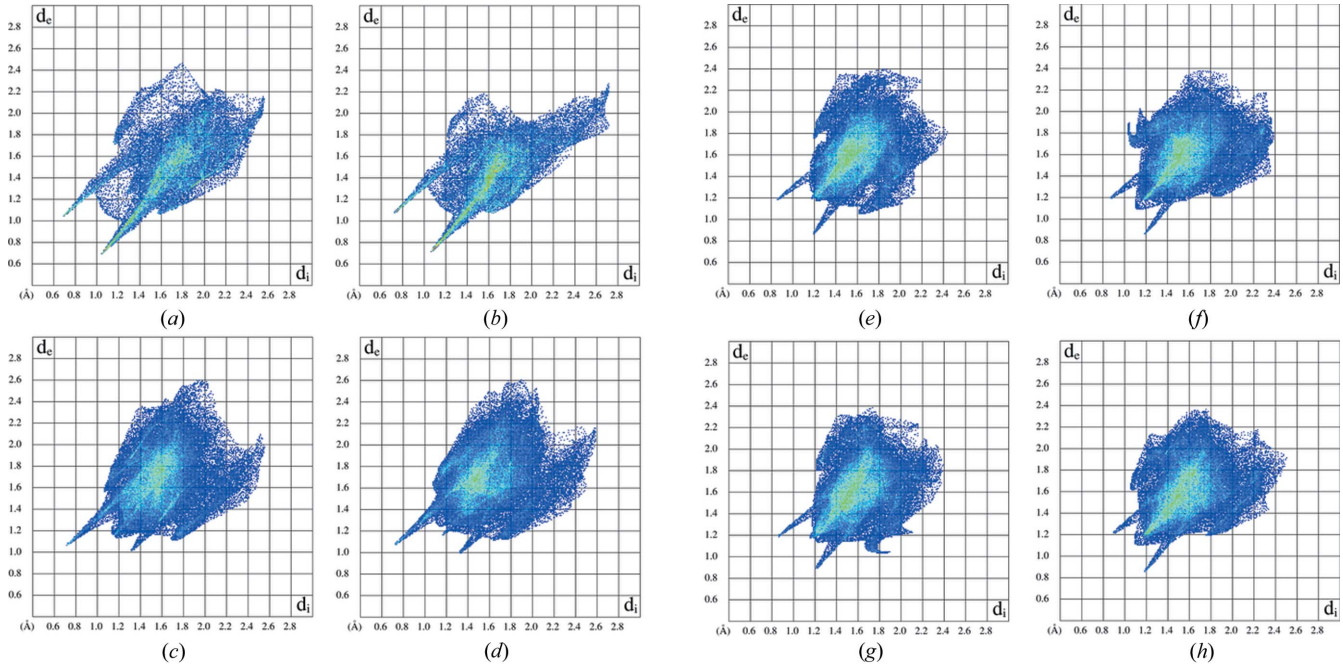

Figure 3
Fingerprint plots for lidbar: barbituric anions (*a*) *A* and (*b*) *B*; two lidocaine cations (*c*) and (*d*); and for lid: four independent lidocaine molecules (*e*) *A*, (*f*) *B*, (*g*) *C* and (*h*) *D*.

Table 2
Polarizability, static first hyperpolarizability tensor components and dipole moment calculated for lidocaine cations (lid_a, lid_b) and barbiturate ions (barb_a, barb_b), melamine molecule (mel), barbital molecule (ba), barbituric acid molecule (bar) and Cubar complexes (O – optimized geometry, E – experimental geometry).

		α_{tot} (Å^3)	β_{tot} (10^{-30} e.s.u.)	μ (D)
lidbar	b3lyp/6-311g(2 d,2p)			
barb_a	O	65.88	0.84	2.17
	E	66.12	1.1	2.53
barb_b	O	65.89	0.84	2.16
	E	66.2	1.07	2.46
lid_a	O	175.1	4.81	10.76
	E	156.91	4.05	12.06
lid_b	O	175.19	5.08	9.74
	E	156.81	4.62	12.04
melba	b3lyp/6-311++g(d,p)			
mel	E	12.65	0.19	0.66
ba	E	17	0.6	1.51
urebar	b3lyp/6-311++g(d,p)			
bar	E	68.81	0.75	0.59
	O	68.58	0.82	0.1
urea	E	33.3	0.93	4.93
	O	33.79	0.79	4.42
Cubar	b3lyp/tzvp			
	E	38.64	190.83	14.25
	O	27.85	208.82	6.54

Table 3
Calculations of $\chi(2)$ tensor components (in pm V^{-1}) for the crystal structures investigated.

	Geometry	λ (nm)	$\chi^{(2)}_{111}$	$\chi^{(2)}_{113}$	$\chi^{(2)}_{122}$	$\chi^{(2)}_{133}$	$\chi^{(2)}_{223}$	$\chi^{(2)}_{333}$
urebar	pb3lyp/6-31g(2d,2p)							
	(*E*)	∞	0.76	1.32	0.02	1.24	0.02	0.01

	Geometry	λ (nm)	$\chi^{(2)}_{112}$	$\chi^{(2)}_{123}$	$\chi^{(2)}_{222}$	$\chi^{(2)}_{233}$
lidbar	pb3lyp/6-31g**					
	(*E*)	∞	0.53	0.65	0.32	0.05

	Geometry	λ (nm)	$\chi^{(2)}_{113}$	$\chi^{(2)}_{223}$	$\chi^{(2)}_{333}$
Cubar	pb3lyp/tzvp				
	(*E*)	∞	0.04	0.10	0.00
melba	pb3lyp/6-31g(2 d,2p)				
	(*E*)	∞	−2.5	0.27	0.64
	RLFTn MP2				
	(*A*)	∞	−5.4	0.3	3.5
		1064	−7.6	0.5	4.9
	(*B*)	∞	−5.5	0.5	2.7
		1064	−8	0.9	4.1
	(*B*)	∞	−6.4	0.8	2.7
		1064	−8.1	0.9	3.4

(Figs. 3*c* and *d*). The only new feature of the fingerprint plots is an additional rounded shape located between two spikes, which indicates short H···H contacts.

In the structure of lidbar, lidocaine ions are arranged in a herringbone motif, which seems to be responsible for the structural polarity. Barbiturate anions form tapes surrounded by lidocaine cations in a pseudo-hexagonal arrangement. It is interesting to compare the crystal structure of lidbar with that of lidocaine (lid). Crystals of lid belong to the $P2_1$ space group, with four independent molecules in the asymmetric unit (Janik, 2009). Crystal data along with details of the refinement are presented in Table 1. The structure was previously solved in the $P2_1/c$ space group with two independent molecules and a substantial disorder (Bambagiotti-Alberti *et al.*, 2007). Lidocaine molecules in the asymmetric unit are connected by four different hydrogen bonds of N—H···O type and by C—H···π interactions. The view along the **b** direction in lidbar and lid structures is presented in Fig. S2. Introducing barbituric anions to the structure causes reorganization of the lidocaine cations, and the creation of new hydrogen-bond motifs. The formation of a structure built from two different species becomes more favorable than the existence of two separate homo-molecular systems. For comparison, fingerprint plots of lidocaine molecules taken from the lid structure are presented in Figs. 3(*e*)–(*h*). The observed variety of shape and color reflects a different percentage share of H···H, O···H and C—H···π interactions in lidocaine molecules, which can be correlated with their unequal conformations. Compared to lidbar there are approximately 10% more H···H contacts (the middle of the drawing) in the structure and the C—H···π interactions are more intense (wing shape motifs, top part of the plot); O···H contacts are again visible as two spikes.

Optical properties of lidbar have been examined by means of *ab initio* calculations and experimental measurements. Static hyperpolarizabilities have been calculated both for the isolated ions at the experimental and optimized geometries using B3LYP/6-31G(2d,2p) and 6-311G(2d,2p) in *GAUSSIAN*09 (Frisch *et al.*, 2009). Bulk properties such as refractive indices, linear and second-order nonlinear electric susceptibilities have been evaluated using the PB3LYP method and 6-31G(2d,2p) basis set as implemented in *CRYSTAL*14 code (Dovesi, Saunders *et al.*, 2014). These results are summarized in Tables 2–4. Comparing values of static hyperpolarizabilities (β_{tot}) of the isolated ions it is evident that lidocaine cations possess *ca* 4 times larger β_{tot} values than barbiturate anions, which indicates their dominant role in the SHG effect. Second harmonic generation efficiency was determined experimentally with the modified Kurtz–Perry technique relative to KDP (Gryl *et al.*, 2013). The observed relative d_{eff} for powdered lidbar is equal to that of KDP: d_{eff} = 1.00 for the 1000 nm laser line or even slightly higher, d_{eff} = 1.15, for the 800 nm line. In order to assess the quality of the crystalline material, crystals of lidbar were examined under the polarized microscope Zeiss Axio.Scope A1 using 100×, 200× and 500× magnification rates. Closer inspection of the crystal habit revealed domain structures characteristic of ferroelectric crystal phases (Fig. 4*a*). The observed interference colors reflect the thickness of the crystal and its birefringence. This unique 'crystal quality' was probably responsible for both difficulties in refractive indices measurements for problems with experimental charge density analysis. Nevertheless, an attempt was made to measure refractive indices for lidbar crystals using the immersion oil method (Hartshorne & Stuart, 1969). This

Table 4
Refractive indices for the examined crystals.

A – optimized geometry B3LYP/6-311+G(d,p), B – optimized geometry PB3LYP/6-31G(d,p), E – experimental.

Method	λ	n_α	n_β	n_γ	$2V$
lidbar					
pb3lyp 6-31g** (E)	∞	1.446	1.506	1.563	85.01n
Experiment		1.54	∼ 1.62	1.67	53.13p
melba					
MP2 (A)	∞	1.652	1.547	1.579	69.7p
	589	1.687	1.571	1.607	70.45p
MP2 (B)	∞	1.664	1.525	1.608	75.14n
	589	1.701	1.547	1.639	74.79n
MP2 charge field (B)	∞	1.67	1.518	1.602	79.89n
	589	1.707	1.539	1.632	79.44n
Periodic b3lyp/6-31g(d,p) (b)	∞	1.574	1.402	1.496	79.77n
Periodic b3lyp/6-31g(2d,2p) (b)	∞	1.6	1.446	1.529	81.26n
Periodic b3lyp/6-31g(2d,2p) (e)	∞	1.531	1.411	1.484	74.08n
Experiment	589	1.587	1.452	1.523	83.22n
Cubar					
pb3lyp/tzvp (e)	∞	1.501	1.622	1.673	61.57n
Experiment		†	1.58	1.70	–
urebar					
pb3lyp/6-31g(2 d,2p) (e)	∞	1.405	1.466	1.549	85.42p

† Value of refractive index could not be determined.

method is based on the observation of bright halo lines (Becke lines) movement. Becke lines are created near the junction between two media – crystal and oil – and their movement can be observed when the image is thrown slightly out of focus. When the refractive index of a crystal matches that of the liquid, the crystal becomes almost invisible, with Becke lines faint and colored as a result of dispersion of n (El-Hinnawi, 1966). Refractive index match is usually done for the Na D-line (λ = 589 nm). Becke line observation shows a yellow–orange line moving into the crystal and a blue line moving into the immersion oil, as the stage of the microscope is lowered against the objective. Crystals of lidbar were immersed in a liquid of known refractive index on a glass slide under the coverslip. Several immersion liquids were tested to determine three refractive indices in different orientations of the crystal:

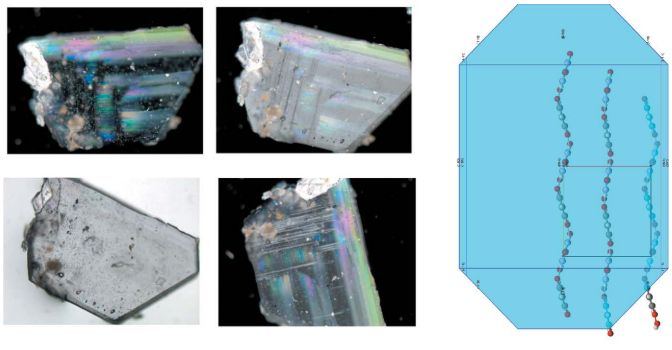

(*a*) (*b*)

Figure 4
(*a*) Crystals of lidbar viewed under the polarizing microscope, (*b*) lidbar crystal morphology.

a mixture of xylene isomers (n_D = 1.496, T = 298 K); a mixture of bromoform (n_D = 1.598, T = 298 K) with methylene iodide (n_D = 1.742, T = 298 K). The prepared sample was then moved under the polarizing microscope and viewed through 100×, 200× and 500× magnification. The optical indicatrix in the monoclinic system has only one axis fixed by symmetry, which coincides with the b axis. Because of the domain nature of the crystal the experimental n_β value could not be determined reliably. Theoretical values of n seem to be slightly underestimated compared with the experimental ones, which could be explained by dispersion effects (experimental values are reported for 598 nm whereas those for ∞ wavelength are theoretical), which seem to be more intense than for other data reported in Table 4. The moderate maximum birefringence of 0.13 can be correlated with the existence of barbiturate tapes with hydrogen bonds of the type N—H···O. The largest value of the refractive index coincides with the crystallographic b axis (Fig. 4*b*).

2.2. Trisaquabis(barbiturato-κO^4)copper(II)

Organic materials modified with inorganic components are interesting from the viewpoint of their outstanding properties as NLO materials as they combine two important features: high SHG response and high damage threshold. It is a real challenge to design a multicomponent material containing API molecules (ensuring appropriate donor–acceptor spatial distribution), an NLO chromophore (with large β hyperpolarizability) and an inorganic skeleton (for good mechanical properties) combined in a noncentrosymmetric crystal structure with dipole moments oriented in one direction. A step towards achieving this goal is designing a two-component crystal structure and when its properties are determined, modifying it with a third component. The structure of 2,2-trisaquabis(barbiturato-κO^4)copper(II), abbreviated as Cubar, was previously reported by Xiong *et al.* (2003), but their method of synthesis and crystallization conditions were different (see supporting information for details). To the best of my knowledge, crystals of Cubar have never been examined from the viewpoint of either optical properties or charge density studies. Selected crystal data and measurement conditions are summarized in Table 5. The structure of Cubar adopts the symmetry of the polar space group *Fdd*2. The asymmetric unit of Cubar is shown in Fig. 5(*a*). The central copper cation and O3 atom, from the water molecule, are both situated on a twofold axis on a special position 8*a* (..2, 0 0 z) of *Fdd*2. Each Cu^{II} cation is coordinated to five O atoms from two barbiturate ions (O6) and three water molecules (O1, O1′, O3) forming a slightly distorted square-pyramidal geometry shown in Fig. 5(*b*). The recognized coordination polyhedra form layers linked by barbiturate anions *via* hydrogen bonds of N—H···O and O—H···O types. Overall there are five crystallographically distinct hydrogen bonds marked *a*–*e* (Table S3). Packing of structural components in Cubar crystals (Figs. 6*a* and *b*) reveals ribbons of barbiturate anions arranged in intersecting tapes. The ribbons are formed by $R_2^2(8)$-type hydrogen-bond motifs and are separated by copper coordi-

Table 5
Data collection, processing, spherical refinement and multipolar refinement for Cubar.

Crystal data	
Chemical formula	$C_8H_{12}N_4O_9Cu$
M_r	371.77
Crystal system, space group	Orthorhombic, *Fdd*2
Temperature (K)	93
a, b, c (Å)	11.6309 (1), 30.2463 (2), 7.1641 (1)
V (Å^3)	2520.27 (4)
Z	8
F(000)	1512
D_x (Mg m^{-3})	1.960
Radiation type	Mo $K\alpha$
μ (mm^{-1})	1.79
Crystal size (mm)	0.23 × 0.13 × 0.09
Data collection	
T_{min}, T_{max}	0.836, 1.053
X-ray power	50 kV, 0.8 mA
Exposure time (s per image)	1 (low 2θ) 40 (high 2θ)
Scan width (°)	1
Total no. of images	3648
Total measurement time	68 h 49 min
Data processing	
Lattice type	*F*
Laue class	*mmm*
θ_{max} (°)	55.73
Resolution (Å^{-1})	1.16
Total no. of reflections	126 673
Completeness (%)	99.9
R merge	0.023
Spherical refinement†	
No. of reflections [unique, >2σ(I)]	8173, 8051
$R1$, wR^2, S	0.0151, 0.0376, 1.131
Flack parameter	0.009 (2)
ρ_{max}, ρ_{min}, r.m.s. (e Å^{-3})	0.427, −0.449, 0.064
Multipolar refinement	
No. of data in refinement [I > 2σ(I)]	8100
$R[F^2>2\sigma(F)]$, $wR(F)$, S	0.011, 0.009, 1.459
Max shift/e.s.d. in last cycle	< 10^{-3}
ρ_{max}, ρ_{min}, r.m.s. (e Å^{-3})	0.263, −0.298, 0.043

† Sheldrick (2015).

nation polyhedra. Detailed graph-set analysis of hydrogen bonds exposed a large number of complicated ring and chain motifs built of hydrogen bonds of O—H···O and/or O—H···N and enclosing Cu polyhedra. An example of two rings of $R_6^6(46)$ and $R_6^6(56)$ can be seen in Figs. 6(*c*) and (*d*).

An experimental charge density study has been conducted in order to provide a deeper insight into the structure and bonding in Cubar. Several low-temperature, high-resolution X-ray diffraction data sets were collected to assess the data quality from different diffractometers. The results of that comparison will be presented elsewhere. In the best dataset low-energy electron contamination of the Mo miscrosource was eliminated by placing a thin aluminium filter in the collimator according to the procedure described by Macchi *et al.* (2011). Emphasis on charge density analysis was placed on the barbiturate ion to determine whether the mesomeric forms of barbituric acid cause the distinction between O6 and O2, O4 atoms resulting in the formation of the Cu—O6 bond. The multipole refinement for Cubar was carried out using the Hansen–Coppens formalism (Hansen & Coppens, 1978) implemented in the *XD*2006 program package (Volkov *et al.*, 2006). The multipole expansion was truncated at the hexadecapole level for Cu atoms, at the octapole level for the C, N and O atoms, and at the dipole level for H atoms. Symmetry restraints were employed on Cu1 and O3 atoms. The choice of local coordination environment is crucial for the appropriate description of the charge-density distribution. In the best model (the smallest *R* values and residual density peaks) *mm*2 local symmetry was applied for the Cu1 and O3 atoms. All pseudoatoms were assigned core and spherical valence densities composed of relativistic wavefunctions reported by Su, Coppens and Macchi (Su & Coppens, 1998; Macchi & Coppens, 2001).

It is well known that the treatment of deformation density of the 3*d* transition metals is challenging due to large differences in radial extensions of 3*d* and 4*s* valence orbitals (Farrugia & Evans, 2005). It is difficult to obtain a reasonable estimate of 4*s* population from the diffraction data as the scattering of 4*s* electrons is only significant in the range (sin θ/λ) < 0.20. This part of the data contains few reflections and tends to be affected by systematic errors. A typical approach is to include the 4*s* population in the core density which is not refined (Farrugia *et al.*, 2008; Scheins *et al.*, 2010). This has been done for Cu atoms in Cubar. Attempts to refine the 4*s* population resulted in a negative charge on the Cu atom and an ambiguous residual density. In the final analysis Cu was treated as a neutral atom with the configuration [Ar]4s^1. The expansion and contraction parameters of the H atoms were fixed at 1.13 for κ and 1.29 for κ' (Volkov *et al.*, 2001). The H-atom anisotropic displacement parameters (a.d.p.s) were estimated by the *SHADE*-2 web server (Madsen, 2006) and the obtained values were subsequently kept

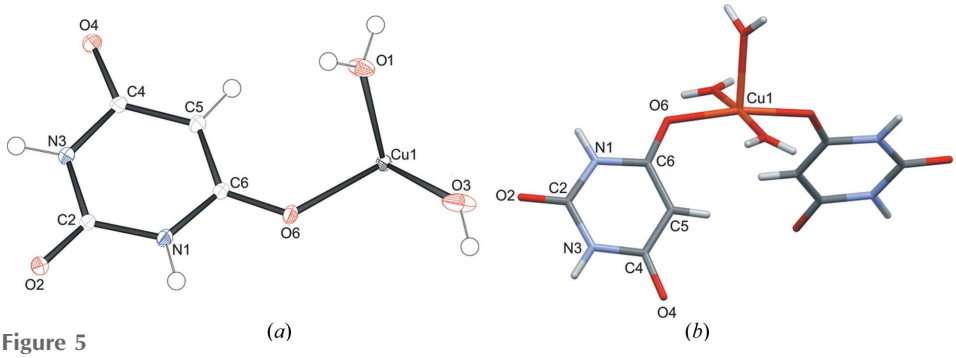

Figure 5
(*a*) Contents of the asymmetric unit of Cubar with the atom-numbering scheme (*ORTEP*3; Farrugia, 1997). Displacement ellipsoids are drawn at 50% probability level. (*b*) The shape of Cu^{II} coordination polyhedron: each Cu atom is coordinated to five O atoms – three from water molecules and two from barbiturate anions. Prepared using *Mercury* (Macrae *et al.*, 2006).

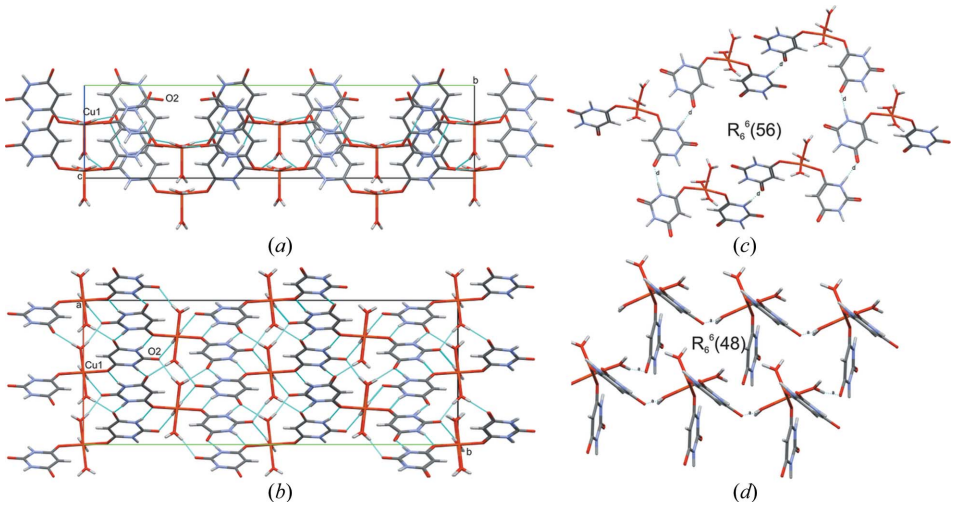

Figure 6
Packing of the Cubar structural components viewed along (*a*) [100] and (*b*) [001]. Barbiturate ions form ribbons separated by Cu^{II} coordination polyhedra. Prepared using *Mercury* (Macrae *et al.*, 2006).

fixed during the refinement. For the O3 atom, situated in a special position, both symmetrically dependent H atoms had to be used to generate a.d.p.s. Each Cu^{II} cation is coordinated to five O atoms forming a slightly distorted square-pyramidal geometry. Four O atoms are located in the square base of the pyramid, whereas the fifth O3 atom is situated in the apex. This specific orientation of ligands is known to lead to an underpopulated $d(x^2 - y^2)$ orbital (Sabino & Coppens, 2003). The population of the Cu^{II} *d*-orbitals was calculated using the d-pop option in *XD*2006. Subsequent searches with either minimal $d(x^2 - y^2)$ or minimal $d(z^2) + d(x^2 - y^2)$ populations confirmed the validity of the chosen model.

The experimental deformation density maps show the typical characteristic features of the static maps. As expected the accumulation of charge density is located in the covalently bonded regions (Fig. 7*a*). The values of charge density along with the Laplacian for the Cu—O bond show that the character of the bonds is intermediate between the closed-shell and shared-shell interaction (Table 6). For the copper interactions with O atoms the values of $\rho(r)$ and $\nabla^2\rho(r)$ are comparable with those reported in the literature for the copper complexes (Farrugia *et al.*, 2008). The slightly lower values of $\rho(r)$ and $\nabla^2\rho(r)$ for Cu1—O3 confirm the Jahn–Teller distortion: the Cu1—O3 bond is much weaker than both Cu1—O6 and Cu1—O1. Laplacian maps (Figs. 7*b* and *c*) indicate the apparent similarities for the O atoms of barbiturate ion O2 and O4. The O6 atom has a different spatial distribution as it is bonded to the copper central atom. These differences in the behavior of carbonyl O atoms might be correlated with the shift of electron density in barbituric acid molecule, prior to the crystal structure formation. The existence of mesomeric forms might be influenced by many factors: the properties of co-crystallizing agents and/or solvent, ionic forces, temperature range, pressure *etc.* It is worth noting that among the three carbonyl O atoms O6 seems to be the most electronegative in that particular environment. The same situation has been observed for other barbiturate complexes (Gryl *et al.*, 2010). This suggests a redistribution of electron density in a barbituric acid molecule towards a mesomeric form *E* prior to crystal structure formation. Bond length analysis does not give a conclusive distinction between the two possible mesomeric forms *E* or *F* (C2═O2 1.24 Å; C4═O4 1.26 Å and C6—O6 1.28 Å).

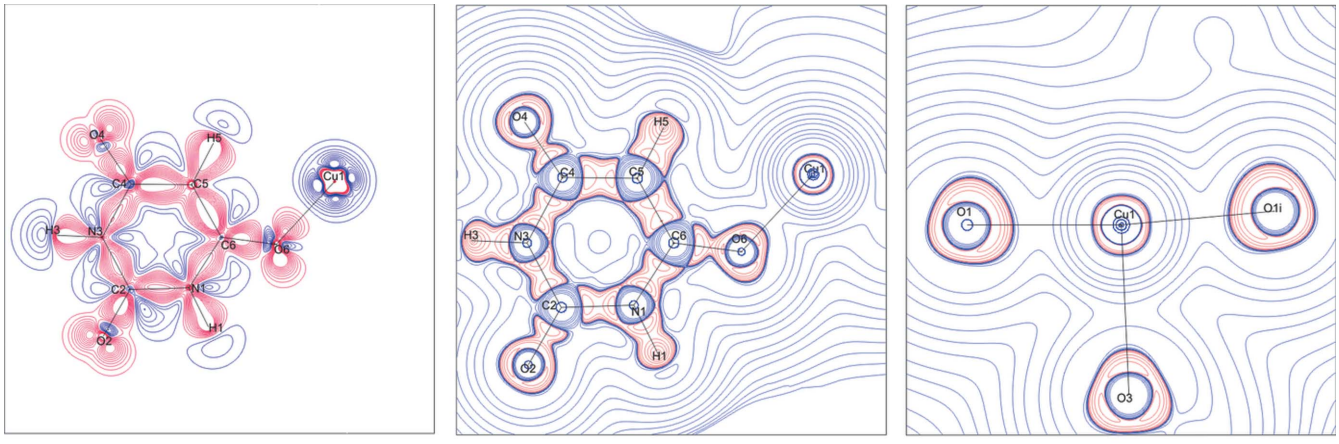

Figure 7
Experimental deformation density static maps in the plane of (*a*) N1—C6—Cu1 for Cubar. Experimental Laplacian maps in the planes of (*b*) N1—C6—Cu1, (*c*) O1—Cu1—O1^{i} [symmetry code: (i) $-\frac{1}{2} - x, \frac{1}{2} - y, z$]. Contours are at logarithmic intervals in $-\nabla^2\rho(r)$ (e Å^{-5}).

Table 6
Experimental topological analysis of bond critical points for Cubar.

$\rho(r)$ (e Å^{-3}) – charge density, Laplacian – $\nabla^2\rho(r)$ (e Å^{-5}) and eigenvalues of Hessian – λ_1, λ_2, λ_3/ (e Å^{-5}), R_{ij} – internuclear separations (Å), d_1, d_2 – distance between BCP and atoms 1 and 2, respectively (Å), ε – ellipticity.

Interaction	$\rho(r)$	$\nabla^2\rho(r)$	R_{ij}	d_1	d_2	λ_1	λ_2	λ_3	ε
Cu1—O6	0.53	10.5	1.978	1.000	0.978	−2.98	−2.86	16.34	0.04
Cu1—O1	0.61	12.19	1.935	0.981	0.954	−3.58	−3.29	19.06	0.09
Cu1—O3	0.34	6.49	2.141	1.089	1.052	−1.74	−1.65	9.88	0.05
O2—C2	2.84	−38.06	1.240	0.766	0.474	−29.33	−23.42	14.69	0.25
O4—C4	2.64	−32.57	1.259	0.771	0.488	−25.41	−22.2	15.04	0.14
O6—C6	2.63	−33.12	1.279	0.784	0.494	−24.4	−22.16	13.44	0.1
N1—C2	2.26	−22.37	1.360	0.777	0.583	−20.93	−15.97	14.53	0.31
N1—C6	2.1	−18.08	1.385	0.788	0.597	−17.83	−14.84	14.58	0.2
N3—C2	2.2	−20.7	1.367	0.779	0.589	−19.64	−15.61	14.55	0.26
N3—C4	2.04	−16.29	1.395	0.794	0.601	−17.38	−14.33	15.41	0.21
C4—C5	2.07	−16.66	1.404	0.729	0.675	−16.59	−12.37	12.3	0.34
C5—C6	2.17	−19.33	1.392	0.723	0.669	−17.69	−13.39	11.75	0.32

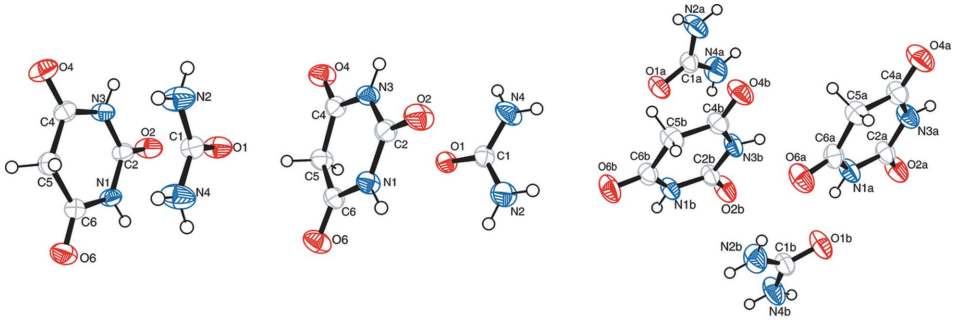

Figure 8
View of the contents of the asymmetric unit with atom-labelling scheme for (*a*) urebar1, (*b*) urebar2 and (*c*) urebar3. Atomic displacement ellipsoids are drawn at the 50% probability level (Gryl *et al.*, 2008).

The Laplacian maps of the Cu atom in different orientations show the three dimensional spatial distribution and shape of the orbitals. Topological properties of the weak interactions are described in Table S3. The weakest hydrogen-bond acceptor is the O6 atom, which is not surprising as O6 is involved in the Cu1—O6 interaction.

Optical properties of Cubar were determined both experimentally and theoretically. Refractive indices have been calculated utilizing the *CRYSTAL*14 code with PB3LYP/TZVP and measured using the immersion oil method using a mixture of xylene isomers (n_D = 1.496, T = 298 K) with bromoform (n_D = 1.598, T = 298 K), and a mixture of bromoform with methylene iodide (n_D = 1.742, T = 298 K). The results are summarized in Table 4. The largest refractive index n_γ coincides with the crystallographic *a* axis, the direction of Cu polyhedra layers. As Cubar crystallizes in the form of thin plates the refractive index n_α was not determined with sufficient accuracy. Calculations of refractive indices provide the information that the crystals of Cubar are biaxial negative with a 2V angle bisected by the smallest refractive index. The maximum birefringence is close to 0.17. Polarizability and hyperpolarizability have been calculated for the complex using the B3LYP method and TZVP basis set. $\chi^{(2)}$ tensor components as well as $d^{(2)}$ tensor components ($d^{(2)} = 1/2\chi^{(2)}$) shown in Table 3 reflect the unfavorable orientation of the dipole moments which almost completely cancel themselves out (Fig. 4). This can be seen by looking at the mutual orientation of barbiturate ligands in the crystal structure. Unfortunately, the bulk SHG effect could not be estimated with the modified Kurtz–Perry technique using 800 and 100 nm excitation due to strong absorption in that region.

2.3. Urea–barbituric acid co-crystal

Among three polymorphic forms of the urea–barbituric acid co-crystal (Fig. 8; Gryl *et al.*, 2008, 2011) the second one is polar (*Cc* space group: urebar2) and thus interesting from the viewpoint of optical properties. The above-mentioned polymorphs are one of a very few examples of synthon polymorphism found in the CSD database according to Mukherjee *et al.* (2011).

Experimental charge density analysis was performed in order to confirm the hypothesis that different mesomeric forms of barbituric acid (Fig. 9) in solution contribute to different utilization of the same hydrogen-bond donor and acceptor sites. The obtained results undermined a belief that the formation of co-crystals limit polymorphism phenomenon (Vishweshwar *et al.*, 2005). Another goal was elucidation of mechanisms underlying the instability of the polar polymorph.

Carbonyl C═O bond-length alternation in urebar2 indicated a shift of electron density towards the known mesomeric form *B* of barbituric acid (Gryl *et al.*, 2008). Topological analysis of charge density including Laplacian maps, electrostatic potential and net atomic charges indicated the distinct accepting properties of the barbiturate O atoms and showed a displacement of electron density towards a mesomeric form of higher stability. It was suggested that the redistribution of charge in the barbituric acid molecule in a particular environment influences the type of hydrogen bond formed and thus the different packing topology observed for the three polymorphs (Gryl *et al.*, 2011). In order to confirm this hypothesis, Laplacian profiles along a O═C bond path have been analysed. Fig. 10 presents a comparison of profiles for O2═C2, O4═C4 and O6═C6 bonds in barbituric acid and O1═C1 bonds in the urea molecule. There are no significant differences between the profiles of O4═C4 and O6═C6 bonds, whereas the O2═C2 bond has altered characteristics.

Bond critical points (BCPs) for O4═C4 and O6═C6 bonds are on the rising slope of the Laplacian both from theory and experiment. O2═C2 bond lengthening causes the redistribution of charge over a wider region, thus BCP can be found at lower values of the Laplacian (Fig. 10). Of course, the altered Laplacian profile for O2═C2 could be explained through dissimilarities in hydrogen-bond accepting properties. The O2 atom is an acceptor of two hydrogen bonds, whereas atoms O4 and O6 form one hydrogen bond each. At a first glance this could explain the apparent similarity between O4 and O6 atoms. We would expect the O1 atom of urea, which also participates as an acceptor of two hydrogen bonds, to be similar to the O2 atom of barbituric acid. However, this is not the case. The Laplacian profile of the O1═C1 bond is more similar to that of O4═C4 and O6═C6 than to O2═C2. This analysis clearly indicates that the resulting hydrogen-bond motifs are an effect of the change in molecular structure of barbituric acid and not the opposite. Values of QTAIM atomic charges and electrostatic potential distribution are both in agreement with this analysis (Gryl *et al.*, 2011). The highest negative charge was found for the O2 atom, whereas the values for O4 and O6 atoms were similar. Differences observed in the electrostatic potential for all three polymorphic forms can be correlated with the intermolecular interactions within the close environment of the appropriate molecules, *e.g.* either barbituric acid or the urea molecule. These specific interactions are indeed a result of the changes in electronic structure of the molecules prior to the crystallization process. Charge density calculations enabled the investigation of the relative stability of all three polymorphic forms of the co-crystal. The electrostatic crystal binding energy was calculated using a combination of the exact potential and multipole methods (EP/MM; Volkov *et al.*, 2004). The global minimum of the lattice energy for the structure corresponds to the most stable polymorphic form. The total binding energy was expressed using the electrostatic exchange–repulsion and dispersion components (Table 7). The experimental and theoretical results are in good agreement: the more stable form appears to be urebar1 ($P2_1/c$) and the less stable form is urebar2 (Cc). Indeed polar crystals left in the matrix solution at room temperature (*ca* 295 K) after several weeks transformed into the form with space group $P2_1/c$, which suggests that the Cc form is thermodynamically less stable. The differentiation of the polymorphs was also made through visualization of intermolecular interactions using Hirshfeld surfaces (Gryl *et al.*, 2011). Fingerprint plots for barbituric acid molecules taken directly from the crystal structures (Fig. 11) confirmed the postulated differences between the molecule in a particular environment in a given polymorphic form. In all forms there can be observed two spikes pointing to the lower left side of the

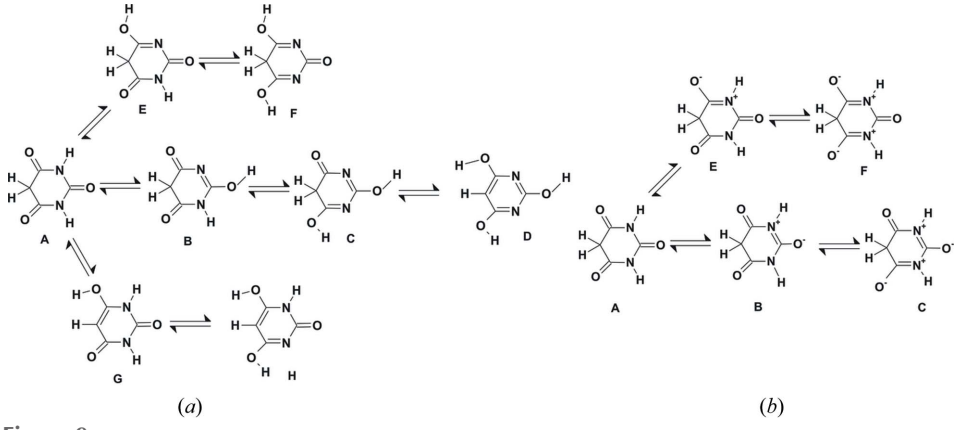

Figure 9
(*a*) Tautomeric forms of barbituric acid; (*b*) mesomeric forms of barbituric acid as derived from the corresponding tautomeric forms (Gryl *et al.*, 2008).

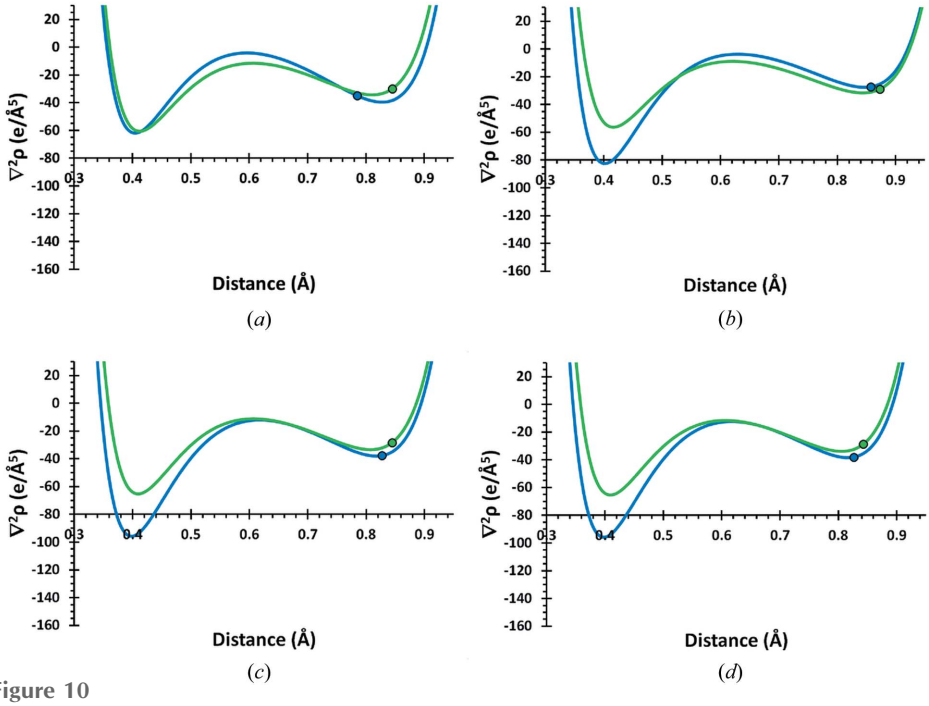

Figure 10
Laplacian profiles along the (*a*) O2═C2, (*b*) O1═C1, (*c*) O4═C4 and (*d*) O6═C6 bonds in urebar2. Green and blue lines refers to the experimental and theoretical data, respectively. The corresponding dots mark the position of the BCP. O atoms are located on the left side of the graphs.

drawing indicating the presence of O···H interactions. Sets of diffuse points between the spikes in urebar1 and even more in urebar2 originate from H···H contacts within the dimers formed by barbiturate ions. The upper wing-shaped features can be attributed to C···H and N···H contacts. By the shape of fingerprint plots we can see a larger variety of interactions seen in urebar1 and urebar2 than in urebar3.

Optical properties calculations were performed at the DFT/B3LYP level using *GAUSSIAN*09 (Frisch *et al.*, 2009) to evaluate molecular polarizabilities, hyperpolarizabilities and dipole moments for urea and barbituric acid molecules. Both components have comparable molecular hyperpolarizabilities, while the dipole moment of urea is several times higher. Preliminary calculations of static refractive indices and the first-order electric susceptibility tensor (χ) for the crystal structure of urebar2 were performed using *CRYSTAL*14 (Dovesi, Saunders *et al.*, 2014). Crystals of urebar2 are biaxial, positive (acute angle between optic axes $2V$ = 85.42°); the refractive indices in the directions of the principle axes are summarized in Table 3. Maximum birefringence is *ca* 0.14. Experimental measurements of SHG and refractive indices were impossible due to the instability of the urebar2 crystals. The small components of the susceptibility tensor are probably due to the antiparallel arrangement of urea and barbituric acid molecules (Fig. 8*b*) causing the apparent weakening of the resultant dipole moment.

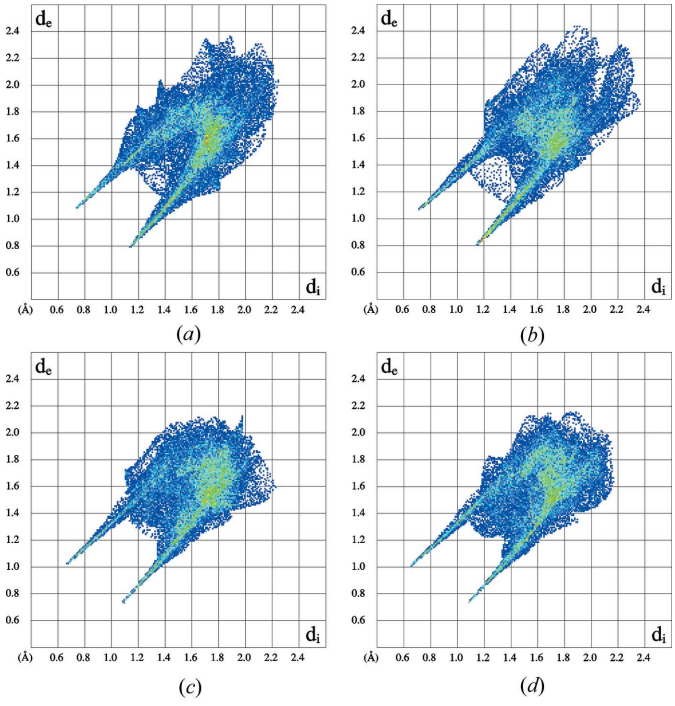

Figure 11
Fingerprint plots of barbituric acid molecule in (*a*) urebar1, (*b*) urebar2, (*c*) urebar3 molecule *A* and (*d*) urebar3 molecule *B*.

Table 7
Total crystal binding energies for the polymorphs. E_{es} – electrostatic crystal binding energy, $E_{ex\text{-}rep}$ – exchange–repulsion crystal binding energy, $E_{energy\text{-}dispersive}$ – dispersion crystal binding energy, E_{int} – total crystal binding energy; all values in kJ mol^{-1}; theoretical values marked in italics.

Total crystal binding energy	E_{es}	$E_{ex\text{-}rep}$	$E_{energy\text{-}dispersive}$	Total
Urebar1 $P2_1/c$	−225.23	262.83	−193.07	−155.51
	−196.16	*190.33*	*−175.94*	−181.77
Urebar2 *Cc*	−169.77	295.09	−194.62	−68.78
	−175.49	203.01	*−181.65*	−146.60

2.4. Melamine barbital addition compound

The final example of an API-based optical material is the melamine barbital co-crystal (melba). Crystal structure, charge density and optical properties of melba have been already examined (Gryl *et al.*, 2014, 2015). The crystal structure is polar with space group $Pmn2_1$. The asymmetric unit consists of half of the building block molecules, as both barbital and melamine occupy positions on the mirror plane (2 *a m* . . of $Pmn2_1$) with z coordinates 0.0 and 0.5, respectively. Mutual orientation of the building blocks determines the observed structural features such as the crinkled tape motifs built of melamine and barbital (Fig. 12*a*), running in the [100] direction, and zigzag like chains, in the [001] direction, formed by barbital molecule hydrophobic side chains (Fig. 12*b*).

Charge-density studies revealed that the formation of melamine barbital co-crystal is the result of two factors: the shift of electron density in a solution towards a mesomeric form of barbital and a lock-key molecular recognition of both barbital and melamine molecules (Gryl *et al.*, 2014).

Fingerprint plots for barbital and melamine in melba (Fig. 13) reflect short O···H and N···H contacts (spikes pointing to the lower left side of the drawing). Sets of diffuse points in between the spikes come from H···H contacts within the dimers formed between melamine and barbital molecules. The single

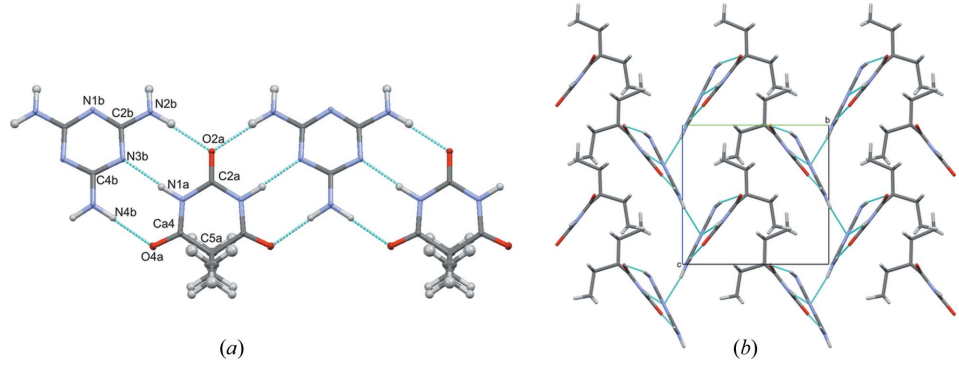

Figure 12
(*a*) Crinkled tapes of melamine and barbital molecules in **melba**. (*b*) Packing of the structural components viewed along [100] with zigzag like chains of barbital molecules (Gryl *et al.*, 2014).

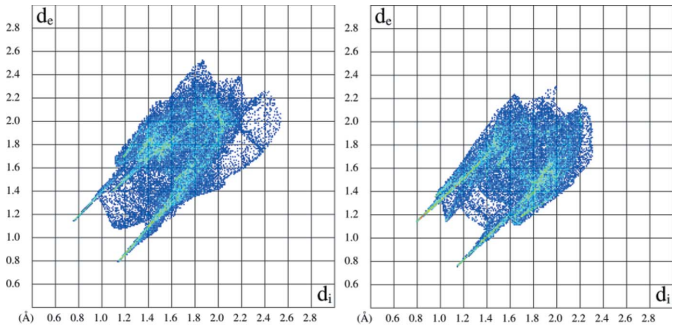

Figure 13
Fingerprint plots of (*a*) barbital molecule and (*b*) melamine in melba.

upper wing-shaped feature for barbital and a single lower wing-shaped feature for melamine can both be attributed to C—H···π interactions. In both plots the central and dominant part of the drawing can be attributed to H···H interactions.

Topological analysis of isolated molecules of melamine and barbital, and the co-crystal indicated the redistribution of electron density towards a mesomeric form *B* of barbital, derived analogously to that of barbituric acid (Fig. 9). The displacement of electron density differentiates the ability of O2*A* and O4*A* to form hydrogen bonds. Net atomic charges calculated using different partitioning schemes, stockholder charges and QTAIM charges showed the same trend of higher charge on O4*A* than on O2*A* confirming the geometrical analysis. Differentiation of O═C bonds in barbital is also visible through the analysis of Laplacian profiles (Fig. 14).

For both O2═C2 and O4═C4 polarization of the bond is more pronounced in the experimental model than in that derived from theory. For C2*A*═O2*A*, bond transition from optimized to experimental geometry results in a changed position of the BCP. Both O2*A* and O4*A* participate in one hydrogen bond each, but O2*A* is engaged in a stronger hydrogen bond. This can be correlated with lengthening of the C═O bond and then electron density is distributed over a wider region with more negative $\nabla^2\rho$ values. In the structure of melba all hydrogen-bond donors and acceptors are engaged in hydrogen-bond formation, except N1*b* which is located in close vicinity to the barbital ring gravity center. Amongst the present hydrogen bonds, N1*a*—H1*a*···N3*b* has an intermediate character between closed- and shared-shell interactions. This could be regarded as competition between N1*a* and N3*b* for the H1*a* atom. The remaining hydrogen bonds of the two fused $R_2^2(8)$ rings act as a clamp enhancing the strength of the N1*a*—H1*a*···N3*b* bond. When comparing the structures of melba and urebar2 the differences between O2 and O4 atoms are less pronounced. However, in both cases of polar co-crystal structures the same mesomeric form *B* of barbital and that of barbituric acid could be recognized.

Optical properties of melba were determined both experimentally (SHG and refractive indices measurements) and theoretically (calculations of molecular polarizabilities, hyperpolarizabilities and linear and second-order nonlinear electric susceptibilities of the molecular crystal). Details of the calculations are presented in Gryl *et al.* (2014). Refractive indices both calculated with and without the use of the charge-polarizing field show relatively good agreement with the values obtained from experiment (Table 4). It is worth noting that introducing an external dressing electric field in the calculations enhances the values of the dipole moment and hyperpolarizability, and causes a decrease in polarizability values. Experimental SHG efficiency measured with a modified Kurtz–Perry method for the powdered sample was *ca* 2 times larger than that of KDP ($d_{\rm eff}$ = 1.86 for the 800 nm excitation line). Phase-matching conditions were determined theoretically with a maximum $d_{\rm eff}$ of *ca* 3 pmV^{-1} (for comparison, the standard SHG measurements for KDP has $d_{\rm eff}$ = 0.35 pm V^{-1}). The key NLO chromophore in melba crystal is barbital with hyperpolarizability ($\beta_{\rm tot}$) 3–4 times larger than for melamine (Table 2). The desired non-centrosymmetric crystal packing is, however, a result of the lock–key molecular recognition of both components. The small geometrical deformation of melamine in the crystal structure with respect to the optimized geometry causes a slight enhancement of the observed bulk effects.

3. Conclusions and future prospects

Directed self-assembly of barbituric acid or its derivatives with organic components possessing suitable donor–acceptor properties or/and with inorganic salts gives the opportunity for novel solutions in non-linear optics. The conducted research proved that combining optical properties in the micro-scale (atoms, molecules) with those of a macro-scale (derived for crystal structure) is crucial for the optimization of crystal engineering methods. Each of the presented materials contributes to understanding API-based crystal phases. In the pure organic materials both component molecules had an impact on the creation of crystal structures. In the mixed organic–inorganic materials the same carbonyl oxygen atom (O6) inter-

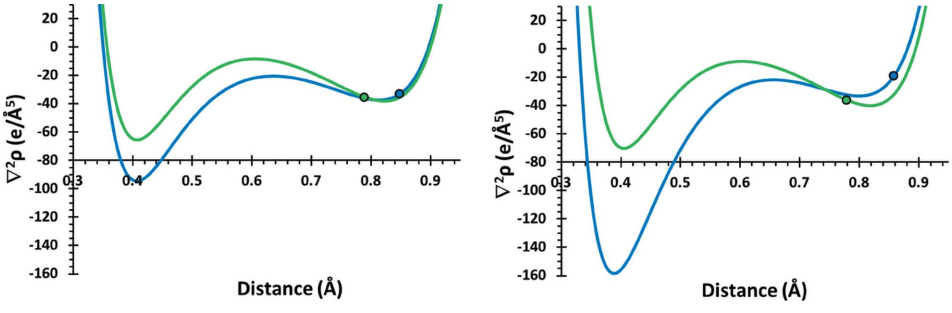

Figure 14
Laplacian profiles along the O2*A*═C2*A* bond of (*a*) barbital and (*b*) C4*A*═O4*A* from the multipolar refinement of experimental (blue line) and theoretical (green line) charge density. The corresponding dots mark the position of the BCP (Gryl *et al.*, 2014).

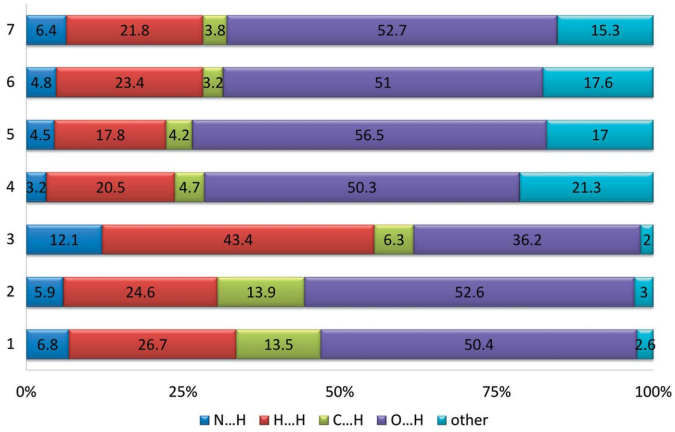

Figure 15
Relative contributions of weak interactions to the Hirshfeld surface area of barbituric acid molecules, barbiturate ions, barbital molecule in the examined structures: 1, 2: barbituric ions in lidbar, 3: barbital molecule in melba, 4, 5, 6, 7: barbituric acid molecule in urebar1, urebar2 and urebar3, respectively.

acts with a central metal ion, which suggests that it is the most electronegative under these conditions. The concomitant analysis of bond lengths and net charges calculated both from experimental and theoretical data showed the influence of the mesomeric forms of barbituric acid and barbital on the creation of specific hydrogen-bond patterns in the studied crystal structures. The relative contributions of weak interactions to the Hirshfeld surface area of barbituric acid molecules, barbiturate ions and barbital molecules in the organic crystals are presented in Fig. 15. Compared with barbiturate moieties there is a considerably larger contribution of H···H interactions in the barbital crystal structure. The percentages of N···H and O···H interactions do not change significantly in the structures containing barbituric acid molecules and barbiturate ions. It is not surprising that in the lidbar structure the ratio of C···H interactions increases at the expense of H···H interactions. Analogously the contribution of N···H interactions in barbital increases and O···H decreases with respect to the remaining crystal structures. The barbituric acid molecule can be considered a better NLO chromophore (Table 1). The barbital molecule shows limited synthon formation flexibility in comparison to barbituric acid as a result of sterical hindrance, and less possibilities for shifting the electron density towards specific mesomeric forms in solution. An attempt to evaluate the optical properties of the selected materials both theoretically and experimentally gave promising results and showed that it is possible to utilize API molecules as building blocks for noncentrosymmetric crystal structures. Introducing molecules with large molecular hyperpolarizabilies – push–pull NLO chromophores – into a known API system is the next step towards obtaining outstanding optical materials.

Acknowledgements

The research was carried out with the equipment purchased thanks to the financial support of the European Regional Development Fund in the framework of the Polish Innovation Economy Operational Program (contract No. POIG.02.01.00-12-023/08). This research was supported in part by PL-Grid Infrastructure. Many thanks to Agilent, in particular Dr Fraser White, for providing the X-ray dataset for Cubar and Professor Katarzyna Stadnicka and Arkadiusz Gryl for fruitful discussions.

References

Andal, C. & Murugakoothan, P. (2014). *Int. J. ChemTech Res.* **6**, 1541–1543.
Bader, R. F. W. (1990). *Atoms in Molecules: A Quantum Theory*. Oxford: Clarendon Press.
Bambagiotti-Alberti, M., Bruni, B., Di Vaira, M., Giannellini, V. & Guerri, A. (2007). *Acta Cryst.* E**63**, o768–o770.
Bisht, K. K., Patel, P., Rachuri, Y. & Eringathodi, S. (2014). *Acta Cryst.* B**70**, 63–71.
Bolz, I., Bauer, M., Rollberg, A. & Spange, S. (2010). *Macromol. Symp.* **287**, 8–15.
Boulanger, B. & Zyss, J. (2003). *International Tables for Crystallography*, Vol. D. Dordrecht: Kluwer Academic Publishers.
Cao, Y.-W., Chai, X.-D., Chen, S.-G., Jiang, Y.-S., Yang, E.-S., Lu, R., Ren, Y.-Z., Blanchard-Desce, M., Li, T.-J. & Lehn, J.-M. (1995). *Synth. Met.* **71**, 1733–1734.
Chimpri, A. S., Gryl, M., Dos Santos, L. H. R., Krawczuk, A. & Macchi, P. (2013). *Cryst. Growth Des.* **13**, 2995–3010.
Chimpri, A. S. & Macchi, P. (2013). *Phys. Scr.* **87**, 048105.
Cole, J. M. (2003). *Philos. Trans. R. Soc. London A*, **361**, 2751–2770.
Dittrich, B., Hübschle, C. B., Luger, P. & Spackman, M. A. (2006). *Acta Cryst.* D**62**, 1325–1335.
Dominiak, P. M., Volkov, A., Li, X., Messerschmidt, M. & Coppens, P. (2007). *J. Chem. Theory Comput.* **3**, 232–247.
Dovesi, R., Orlando, R., Erba, A., Zicovich-Wilson, C. M., Civalleri, B., Casassa, S., Maschio, L., Ferrabone, M., De La Pierre, M., D'Arco, P., Noël, Y., Causà, M., Rérat, M. & Kirtman, B. (2014). *Int. J. Quantum Chem.* **114**, 1287–1317.
Dovesi, R., Saunders, V. R., Roetti, C., Orlando, R., Zicovich-Wilson, C. M., Pascale, F., Civalleri, B., Doll, K., Harrison, N. M., Bush, I. J., D'Arco, P., Llunell, M., Causà, M. & Noël, Y. (2014). *CRYSTAL*14 User's Manual. University of Torino, Italy.
El-Hinnawi, E. E. (1966). *Methods in Chemical and Mineral Microscopy*. Amsterdam: Elsevier.
Espinosa, E., Souhassou, M., Lachekar, H. & Lecomte, C. (1999). *Acta Cryst.* B**55**, 563–572.
Farrugia, L. J. (1997). *J. Appl. Cryst.* **30**, 565.
Farrugia, L. J. & Evans, C. (2005). *J. Phys. Chem. A*, **109**, 8834–8848.
Farrugia, L. J., Middlemiss, D. S., Sillanpää, R. & Seppälä, P. (2008). *J. Phys. Chem. A*, **112**, 9050–9067.
Feng, J.-D., Yan, L.-K., Su, Z.-M., Kan, Y.-H., Lan, Y.-Q., Liao, Y. & Zhu, Y.-L. (2006). *Chin. J. Chem.* **24**, 119–123.
Frisch, M. J. *et al.* (2009). *GAUSSIAN*09, Revision A.1. Gaussian Inc., Wallingford, CT, USA.
Garín, J., Orduna, J., Rupérez, J. I., Alcalá, R., Villacampa, B., Sánchez, C., Martín, N., Segura, J. L. & González, M. (1998). *Tetrahedron Lett.* **39**, 3577–3580.
Geetha, D., Prakash, M., Caroline, M. L. & Nadu, T. (2011). *Adv. Appl. Sci. Res.* **2**, 86–92.
Gryl, M., Cenedese, S. & Stadnicka, K. (2015). *J. Phys. Chem. C*, **119**, 590–598.
Gryl, M., Kozieł, M., Stadnicka, K., Matulková, I., Němec, I., Tesařová, N. & Němec, P. (2013). *CrystEngComm*, **15**, 3275–3278.
Gryl, M., Krawczuk, A. & Stadnicka, K. (2008). *Acta Cryst.* B**64**, 623–632.
Gryl, M., Krawczuk-Pantula, A. & Stadnicka, K. (2010). *Acta Cryst.* A**66**, s286–s287.

Gryl, M., Krawczuk-Pantula, A. & Stadnicka, K. (2011). *Acta Cryst.* B**67**, 144–154.
Gryl, M., Seidler, T., Stadnicka, K., Matulková, I., Němec, I., Tesařová, N. & Němec, P. (2014). *CrystEngComm*, **16**, 5765–5768.
Hansen, N. K. & Coppens, P. (1978). *Acta Cryst.* A**34**, 909–921.
Hartshorne, N. H. & Stuart, A. (1969). *Practical Optical Crystallography.* London: Arnold.
Hathwar, V. R., Pal, R. & Guru Row, T. N. (2010). *Cryst. Growth Des.* **10**, 3306–3310.
Hathwar, V. R., Thakur, T. S., Row, T. N. G. & Desiraju, G. R. (2011). *Cryst. Growth Des.* **11**, 616–623.
Howard, S. T., Hursthouse, M. B., Lehmann, C. W., Mallinson, P. R. & Frampton, C. S. (1992). *J. Chem. Phys.* **97**, 5616–5630.
Hübschle, C. B., Luger, P. & Dittrich, B. (2007). *J. Appl. Cryst.* **40**, 623–627.
Janik, A. (2009). PhD thesis, Kraków, Jagiellonian University.
Jelsch, C., Pichon-Pesme, V., Lecomte, C. & Aubry, A. (1998). *Acta Cryst.* D**54**, 1306–1318.
Kondo, K., Fukutome, N., Ohnishi, N., Aso, H., Kitaoka, Y. & Sasaki, T. (1991). *Jpn. J. Appl. Phys.* **30**, 3419–3420.
Kondo, K., Ochiai, S., Takemoto, K. & Irie, M. (1990). *Appl. Phys. Lett.* **56**, 718.
Kondo, K., Ochiai, S., Takemoto, K., Kai, Y., Kasai, N. & Yoshida, K. (1992). *Chem. Phys. Lett.* **188**, 282–286.
Krawczuk, A. & Macchi, P. (2014). *Chem. Central J.* **8**, 68.
Lee, S. M., Jahng, W. S., Lee, J. H., Rhee, B. K. & Park, K. H. (2005). *Chem. Phys. Lett.* **411**, 496–500.
Lehn, J., Mascal, M., Decian, A. & Fischer, J. (1990). *J. Chem. Soc. Chem. Commun.* pp. 479–481.
Macchi, P., Bürgi, H.-B., Chimpri, A. S., Hauser, J. & Gál, Z. (2011). *J. Appl. Cryst.* **44**, 763–771.
Macchi, P. & Coppens, P. (2001). *Acta Cryst.* A**57**, 656–662.
Macrae, C. F., Edgington, P. R., McCabe, P., Pidcock, E., Shields, G. P., Taylor, R., Towler, M. & van de Streek, J. (2006). *J. Appl. Cryst.* **39**, 453–457.
Madsen, A. Ø. (2006). *J. Appl. Cryst.* **39**, 757–758.
Mallinson, P. R., Smith, G. T., Wilson, C. C., Grech, E. & Woźniak, K. (2003). *J. Am. Chem. Soc.* **125**, 4259–4270.
Matta, C. F. & Bader, R. F. W. (2006). *J. Phys. Chem. A*, **110**, 6365–6371.
McKinnon, J. J., Jayatilaka, D. & Spackman, M. (2007). *Chem. Commun.* pp. 3814–3816.
McKinnon, J. J., Mitchell, A. S. & Spackman, M. A. (1998). *Chem. Eur. J.* **4**, 2136–2141.
Mukherjee, A., Grobelny, P., Thakur, T. S. & Desiraju, G. R. (2011). *Cryst. Growth Des.* **11**, 2637–2653.
Munshi, P. & Row, T. N. G. (2005). *J. Phys. Chem. A*, **109**, 659–672.
Pal, S. K., Krishnan, A., Das, P. K. & Samuelson, A. G. (2001). *J. Organomet. Chem.* **637–639**, 827–831.
Pandey, J. R. (2014). *AJER*, **3**, 30–36.
Rai, R., Ramasamy, P. & Lan, C. (2002). *J. Cryst. Growth*, **235**, 499–504.
Ratajczak, H. M., Bryndal, I., Ledoux-Rak, I. & Barnes, A. J. (2013). *J. Mol. Struct.* **1047**, 310–316.
Ruby, A. & Raj, S. A. C. (2013). *Chemtech*, **5**, 482–490.
Sabino, J. R. & Coppens, P. (2003). *Acta Cryst.* A**59**, 127–131.
Scheins, S., Zheng, S.-L., Benedict, J. B. & Coppens, P. (2010). *Acta Cryst.* B**66**, 366–372.
Seidler, T., Stadnicka, K. & Champagne, B. (2014). *Adv. Opt. Mater.* **2**, 1000–1006.
Senthil, S., Pari, S., Joseph, G. P., Sagayaraj, P. & Madhavan, J. (2009). *Physica B*, **404**, 2336–2339.
Senthil Murugan, G. & Ramasamy, P. (2015). *Opt. Mater.* **46**, 504–509.
Sheldrick, G. M. (2015). *Acta Cryst.* C**71**, 3–8.
Song, O. K., Wang, C. H., Cho, B. R. & Je, J. T. (1995). *J. Phys. Chem.* **99**, 6808–6811.
Stadnicka, K., Milart, P., Olech, A. & Olszewski, P. K. (2002). *J. Mol. Struct.* **604**, 9–18.
Su, Z. & Coppens, P. (1998). *Acta Cryst.* A**54**, 646–652.
Tiekink, E. R. T., Vittal, J. J. & Zaworotko, M. (2011). *Organic Crystal Engineering. Frontiers in Crystal Engineering.* Chichester: John Wiley and Sons, Ltd.
Toth, S. J., Schmitt, P. D., Snyder, G. R., Trasi, N. S., Sullivan, S. Z., George, I., Taylor, L. S. & Simpson, G. J. (2015). *Cryst. Growth Des.* **15**, 581–586.
Vishweshwar, P., McMahon, J., Peterson, M. L., Hickey, M. B., Shattock, T. R. & Zaworotko, M. J. (2005). *Chem. Commun.* pp. 4601–4603.
Vohra, V., Suresh, S., Ponrathnam, S., Rajan, C. R. & Kajzar, F. (2000). *J. Polym. Sci. Part A Polym. Chem.* **38**, 962–971.
Volkov, A., Abramov, Y. A. & Coppens, P. (2001). *Acta Cryst.* A**57**, 272–282.
Volkov, A., Li, X., Koritsanszky, T. & Coppens, P. (2004). *J. Phys. Chem. A*, **108**, 4283–4300.
Volkov, T., Macchi, P., Farrugia, L. J., Gatti, C., Mallinson, P., Richter, T. & Koritsanszky, T. (2006). *XD*2006. University at Buffalo, State University of New York, NY, USA; University of Milano, Italy; University of Glasgow, UK; CNRISTM, Milano, Italy; Middle Tennessee State University, TN, USA.
Volkov, A., Messerschmidt, M. & Coppens, P. (2007). *Acta Cryst.* D**63**, 160–170.
Whitten, A. E., Turner, P., Klooster, W. T., Piltz, R. O. & Spackman, M. (2006). *J. Phys. Chem. A*, **110**, 8763–8776.
Xiong, Y., He, C., An, T., Cha, C., Zhu, X. & Jiang, S. (2003). *Trans. Met. Chem.* **28**, 69–73.
Zarychta, B., Pichon-Pesme, V., Guillot, B., Lecomte, C. & Jelsch, C. (2007). *Acta Cryst.* A**63**, 108–125.
Zerkowski, J. A., MacDonald, J. C. & Whitesides, G. M. (1997). *Chem. Mater.* **9**, 1933–1941.